J Mater Sci: Mater Electron (2022) 33:12638–12647

Egg white-mediated synthesis of $BiFeO_3$ cubes and their enhanced photocatalytic degradation properties under solar irradiation

S. Bharathkumar[1], M. Sakar[1,2], and S. Balakumar[1,*]

[1] National Centre for Nanoscience and Nanotechnology, University of Madras, Guindy Campus, Chennai, Tamil Nadu 600025, India
[2] Centre for Nano and Material Sciences, Jain University, Bangalore, Karnataka 562112, India

Received: 4 December 2021
Accepted: 5 April 2022
Published online: 26 April 2022

ABSTRACT

Herein, the egg white-mediated synthesis of $BiFeO_3$ (BFO) cubes has been demonstrated using it as metal complex-forming agent during the sol–gel process. The $BiFeO_3$ phase is confirmed using XRD technique, while the XPS spectra confirmed the native oxidation state of the elements and chemical composition. The XPS studies also showed that synthesized BFO particles via conventional sol–gel method possess oxygen vacancies, while no such defect is observed in BFO cubes. The cubic morphology with average size of 150 nm is observed from their FESEM images, while irregular particles of size around 300 nm is observed for BFO synthesized via conventional sol–gel process. The bandgap energy of particles and cubes is estimated to be around 2.32 and 2.36 eV, respectively, and the observed reduced bandgap energy could be due to the defects induced new energy level in BFO particles, while the increased bandgap energy of BFO cubes is attributed to their discrete band energy structure due to their uniform cubic morphology. The solar-driven photocatalytic efficiency toward degradation of methylene blue (MB) dye is found to be enhanced for BFO cubes (99.6%) as compared to particles (73.2%) at the end of 3 h, which attributed to the existence of improved charge separation, recombination resistance, rich surface-active sites, and suitable redox potential in BFO cubes as corroborated from their XPS, PL, and scavenger studies. The photocatalytic recyclability tests up to 5 cycles indicated that BFO cubes is photochemically stable and can be employed for durable photocatalytic degradation applications.

Address correspondence to E-mail: balasuga@yahoo.com

https://doi.org/10.1007/s10854-022-08213-w

1 Introduction

In recent times there is a spotlight on bismuth ferrite ($BiFeO_3$/BFO) owing to its unique and excellent multiferroic properties [1, 2]. BFO is a single-phase perovskite (ABO_3) structured compound that exhibits simultaneous ferroelectric and G-type antiferromagnetic properties in room temperature with Neel temperature of 643 K and Curie temperature of 1103 K [3–5]. It is considered as an interesting material due to the origin such as the 6 s lone pair electrons of Bi^{3+} ions are responsible for ferroelectricity [6], while the magnetic ordering originates due to the partially occupied *d* orbital in Fe^{3+} ions [7]. In addition to its multiferroic-based applications, BFO is also a visible light-driven photocatalytic material that largely explored for organic pollutant degradation and water splitting applications [8].

Organic dyes and pharmaceutical molecules such as antibiotics pose a serious threat to the environment due to their non-degradable nature, carcinogenic nature, and toxic impacts on the soil, water, and air [9, 10]. Toward addressing such issues, the oxidation techniques such as advanced oxidation process (AOP) can be helpful in degrading these harmful chemicals into harmless products such as CO_2 and H_2O [11, 12]. In this direction, semiconductor photocatalysts are used as an activator to conduct this advanced oxidation process and these semiconductor photocatalysts can be ideal systems due to their non-toxic and low cost in nature, where their properties can be also easily tuned via doping, composite formation, size, and shape controlling of the particles [13–15].

Considering the perovskite-based materials, it is largely demonstrated that the controlling of 'A' and/or 'B' sites through doping or by influencing the particle size and shape can lead to the modifications in the overall properties of the material [16]. For instance, it is demonstrated in BFO that the change of material structure from particle (3D) to fiber (1D) can enhance the electrical and magnetic properties via delocalization of electrons and via tuning the canted spin structures, respectively, in BFO [17, 18]. Therefore, synthesis of BFO with different morphologies such as flowers [19, 20], fibers [21, 22], sheets [23], and rods [24] can be a straight forward approach to enhance its properties for the given applications [25–27]. The egg white synthesis of nanomaterials has been proposed as a low-cost and biologically friendly alternate to chemical and physical methods [28, 29]. It is known that the egg white is a biological viscous liquid that has important biomolecules such as amino acids and proteins such as albumin and lysosome [30]. These molecules help material to have highly reactive surfaces due to their surface functionalization effect and size/shape controlling effect during the growth of nanomaterials [31]. This ultimately results in enhancing the properties of nanomaterials, especially, the photocatalytic properties in the present case. In this context, herein, we have demonstrated the synthesis of BFO using egg white as metal complex agent in sol–gel process and obtained the BFO particle with cubic morphology, whereas the conventional sol–gel process yielded the BFO particles with irregular shapes. The comparative studies of these morphologies showed that the properties of BFO can be enhanced by changing its shape from irregular shape to cubic shape which possibly alters the band structure via the morphology-induced confinements in the system.

2 Experiment

2.1 Material synthesis

In the typical sol–gel procedure, 1:1 ratio of nitrate of bismuth and iron ($Bi(NO_3)_3$ $5H_2O$ and $Fe(NO_3)_3$-$9H_2O$) was dissolved in 15 mL of double distilled (DD) water using a magnetic stir. To this, 1 mL of 70% conc. HNO_3 was added to attain a transparent solution. Then, tartaric acid at an optimized ratio of 1:2 with respect to the metal ions was added to the above solution for the gelling purposes. The obtained mixture was heated at 80 °C for 2 h under stirring and dried to powders. The final product was grinded into a fine powder using mortar and pestle and calcinated at 600 °C for 2 h in order to achieve pure phase $BiFeO_3$. The same process was repeated to prepare the BFO cubes, wherein the 10 mL of egg white was used as gelling agent instead of tartaric acid.

2.2 Materials characterizations

X-ray diffraction (XRD) analysis was carried out using Cu Kα (XRD-Analytical Instruments). Morphological images on the prepared samples were taken using field-emission (FE) scanning electron

microscope (FESEM from Hitachi HighTech SU6600); elemental composition and chemical valence state of the atomic elements in the samples were analyzed using X-ray photoelectron spectroscopy instrument from Scienta Omicron-Nanotechnologies. The photoluminescence (PL) spectrometer from HORIBA Jobin Yvons Lab and UV–Vis diffuse reflectance spectrometer (UV–Vis Abs/DRS-Perkin Elmer) techniques were employed for optical property analyses.

2.3 Photocatalytic experiment

The photocatalytic properties of the synthesized BFO particles and cubes on their efficiency toward degradation of methylene blue (MB) dye were examined under direct sunlight exposures. In the typical investigation, 10 ppm MB solution was prepared as a stock. 100 mL of this dye-solution was taken and 50 mg of photocatalyst was dispersed. Then, the mixture was kept under stirring in dark for 30 min to attain the sorption equilibrium. Finally, the solution was irradiated with sunlight and the degradation of MB was observed in timed period using UV–Visible spectrometer. The intensity of sunlight was measured using a digital Lux meter (LT-LutronLX-10/A, TES Electrical Electronic Corp., Taiwan), and the average lux was measured to be $\sim 11 \times 10^4 \pm 100$ lx. The same experimental protocol was used during recycle test, which is conducted for 5 cycles.

3 Result and discussion

3.1 Phase and structure analysis

The phase confirmation of the synthesized BFO particles and cubes was executed using X-ray diffraction technique and the obtained patterns are given in Fig. 1a, b. The diffraction peaks are observed to be well matched with standard JCPDS data #71-2494, wherein the crystal system of the formed particles and cubes was found to be single-phase $BiFeO_3$ perovskite material with rhombohedral system in R3*c* space-group [32, 33]. It should be noted that there is no additional and/or secondary phase observed in the patterns, which indicates that the formed materials are impurity/secondary phase-free systems. The crystallite size of the prepared BFO particles and cubes was estimated using the basic Scherrer's equation [1] corresponding to the doublet peaks (104) and (110) and found to be $\sim$ 26 and $\sim$ 33 nm.

$$D = \frac{K\lambda}{\beta \cos\theta} \quad (1)$$

where D is the average crystallite size, λ is the X-ray wavelength, β is the full width at half maximum (FWHM), θ is the Bragg angle, and K is crystallite shape constant, which is 0.9 corresponding to spherical shape of the crystallites. Furthermore, the lattice parameters such as ($a = b$, c) and volume (V) are calculated using the X'pert HighScore software equipped in the XRD instrument and the obtained values are given in Table 1.

3.2 Morphological analysis

The morphology of synthesized BFO samples is analyzed using FESEM and the acquired images are displayed in Fig. 2a–d. It can be seen that the morphology of BFO synthesized using tartaric acid is found to be irregular and agglomerated structure with particle size ranging from 250 to 500 nm, whereas the egg white-synthesized BFO is found to be with cubic morphology with size ranging from 80 to 200 nm. The observed cubic morphology of the material can be directly attributed to the egg white used as a gelling agent in the synthesis process. Egg white essentially a viscous and protein-rich liquid and contains other biomolecules that act as a matrix for the controlled growth the of BFO crystals [34, 35]. The cubic morphology could be originated due to the shape-directing behavior of the biomolecules present in the egg white. It is clear that the use of egg white can be effective in terms of controlling the particle size and shape of BFO materials and especially, it can be a suitable alternative gelling agent for the partial green synthesis of BFO nanostructures [36].

3.3 Chemical valence state analysis

The elemental compositions and chemical valence state of the atomic elements in the prepared BFO particles and cubes were investigated via XPS and the obtained spectra of the individual elements are given in Fig. 3a–d. The survey spectra as shown in Fig. 3a confirm the presence of all the required elements in the system and the absence of any other elements suggested that the formed BFO materials are impurity-free as corroborated from their XRD patterns.

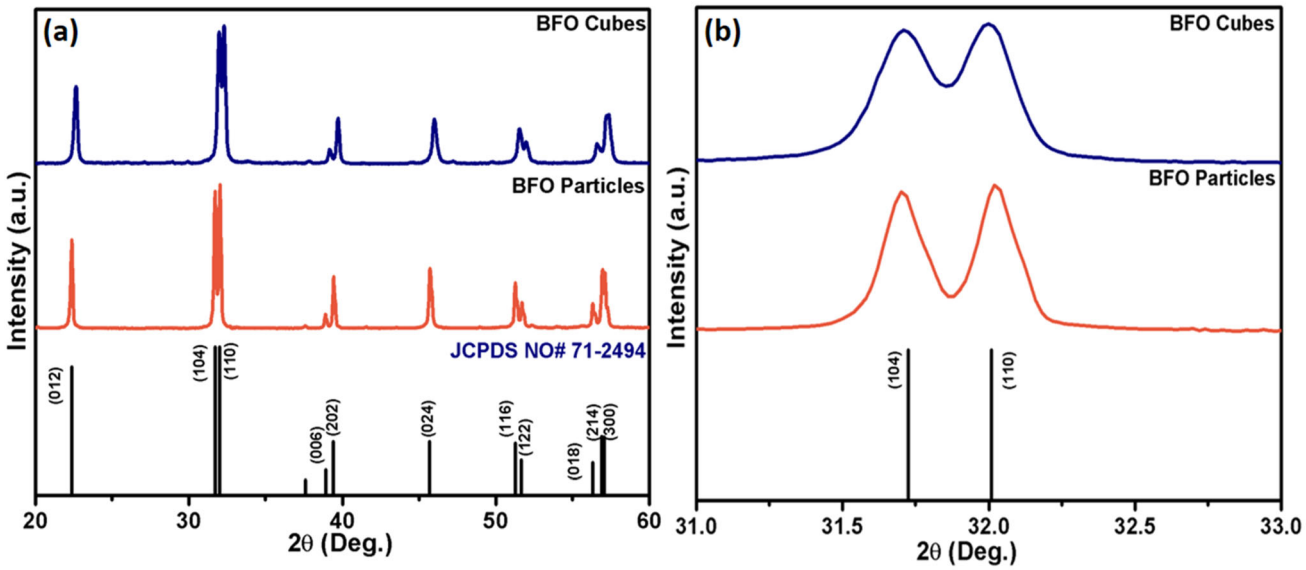

Fig. 1 **a** XRD result of BFO particles and cubes and **b** zoom-in pattern showing the shift in the doublet peaks with respect to the JCPDS data

Table 1 Estimated lattice parameters of BFO particles and cubes

Sample	*a* (Å)	*b* (Å)	*c* (Å)	Cell volume (*V*) (Å^3)
BFO particles	5.5932	5.5932	13.925	378.42
BFO cubes	5.5847	5.5847	13.893	374.20

The core-level XPS spectra of Bi 4f (Fig. 3b) show the binding energy peaks of Bi $4f_{7/2}$ and Bi $4f_{5/2}$ at 158.7 eV and 163.8 eV for particles and 158.3 eV and 163.5 eV for cubes, respectively [37]. This suggests that the oxidation state of Bi in both system is + 3. Similarly, the major peaks appeared at 710.6 eV and 724.4 eV for particles and 711.8 eV and 725.4 eV for cubes corresponding to Fe $2p_{3/2}$ and Fe $2p_{1/2}$ [38], respectively, as shown in Fig. 3c, which indicates that both the systems possess Fe ions with + 3 oxidation state. However, the relative suppression of satellite peak for BFO particles indicates that there could be Fe ions with mixed valance states such Fe^{3+} and Fe^{2+}. This suggests that there could be oxygen vacancies in the system, which is further confirmed from their O 1s XPS spectra as shown in Fig. 3d.

The peak corresponding to O 1s peak indicating the lattice oxygen (O_L) in the system is appeared at 529.1 and 529.8 eV for particles and cubes, respectively [39]. The peak profile of BFO particles shows relatively an asymmetric hump in the lower binding energy and the relative shift of O_L peak at 529.1 eV indicates that the BFO particles possess oxygen vacancies, whereas the O 1s profile of BFO cubes is found to be symmetric with appropriate metal–oxygen binding energy indicates that there is no or well below threshold oxygen vacancies in the system. Accordingly, it can be correlated that the deconvoluted peak corresponding to chemisorbed oxygen species (O_C) is relatively pronounced for BFO particles (at 533.9 eV) as compared to BFO cubes (533.3 eV). This further corroborates the existence of oxygen vacancies in BFO particles as compared to BFO cubes.

3.4 Optical properties

The bandgap energy of the prepared BFO particles and cubes is calculated using their UV–Visible diffuse reflectance spectroscopy via Kubelka–Munk (KM) plots as displayed in Fig. 4a. From the obtained KM plot, the bandgap energy of BFO particles and cubes is estimated to be around 2.32 and 2.36 eV, respectively. In BFO, the bandgap structure is composed of the overlying of Fe 3*d* and O 2*p* states. Therefore, the relative presence of oxygen vacancies in the system can create a vacancy energy level just above the valence band maximum in BFO particles and thus it slightly reduced the bandgap energy of the system [40]. Furthermore, the energy levels in these cubic structures can be discrete and caused a blue shift in the optical property, leading to relatively

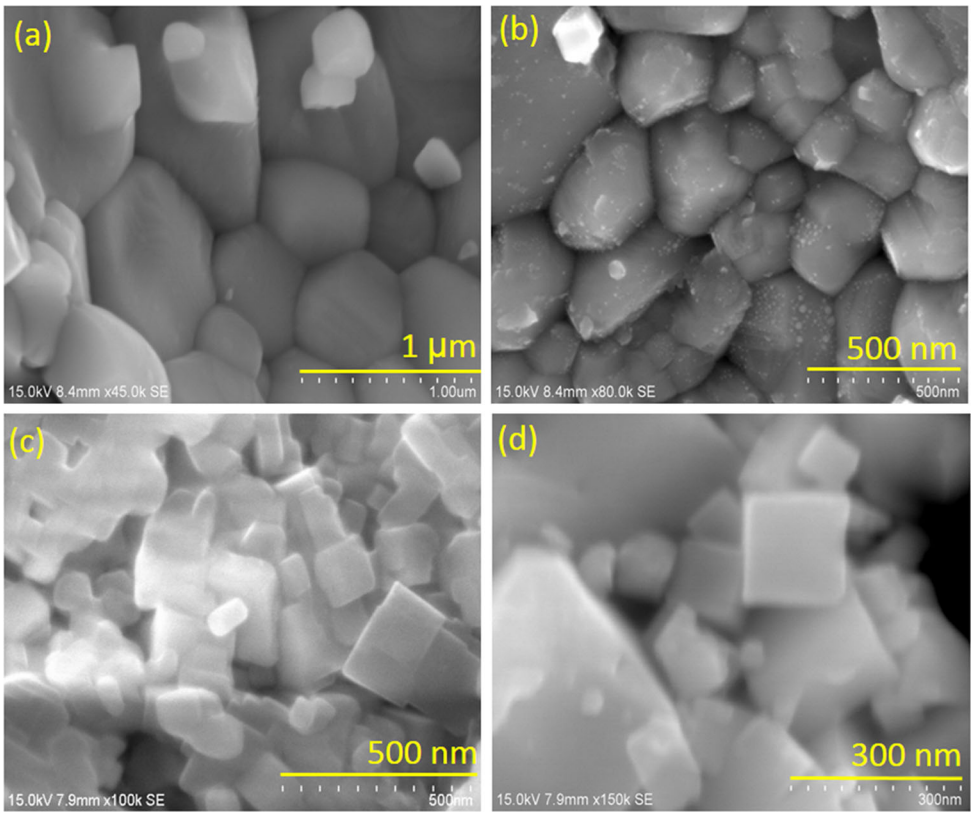

Fig. 2 FESEM micrographs of BFO **a** and **b** particles and **c** and **d** cubes

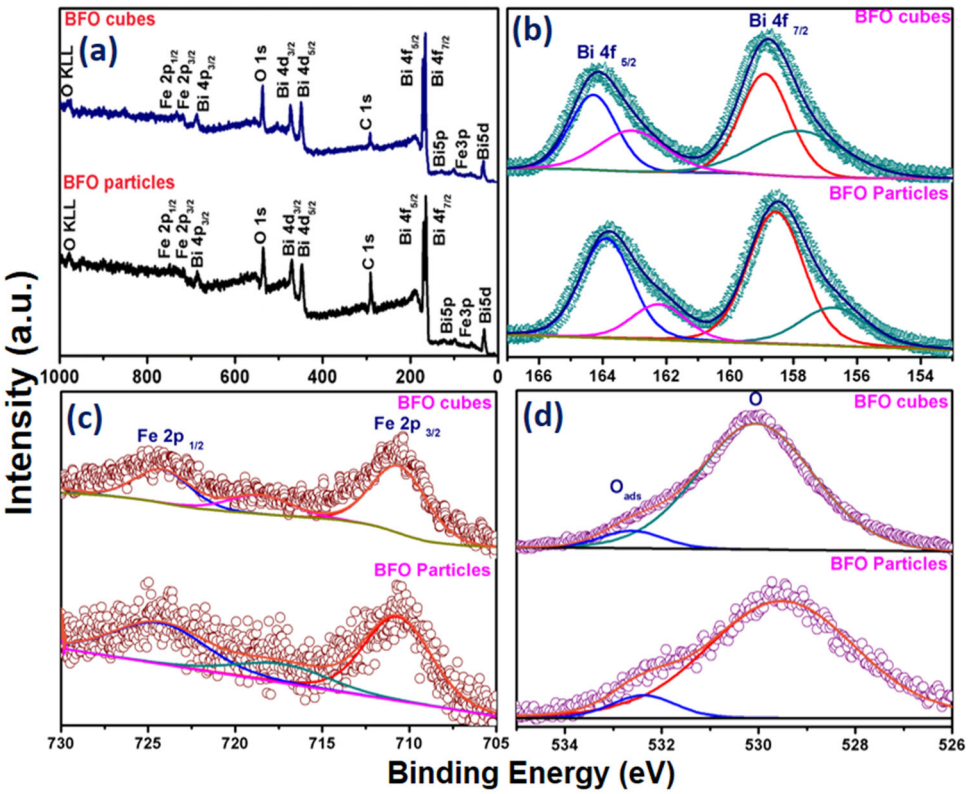

Fig. 3 **a** XPS survey spectrum and narrow scan spectra of **b** Bi 4f, **c** Fe 2p and **d** O 1 s of BFO particles and cubes

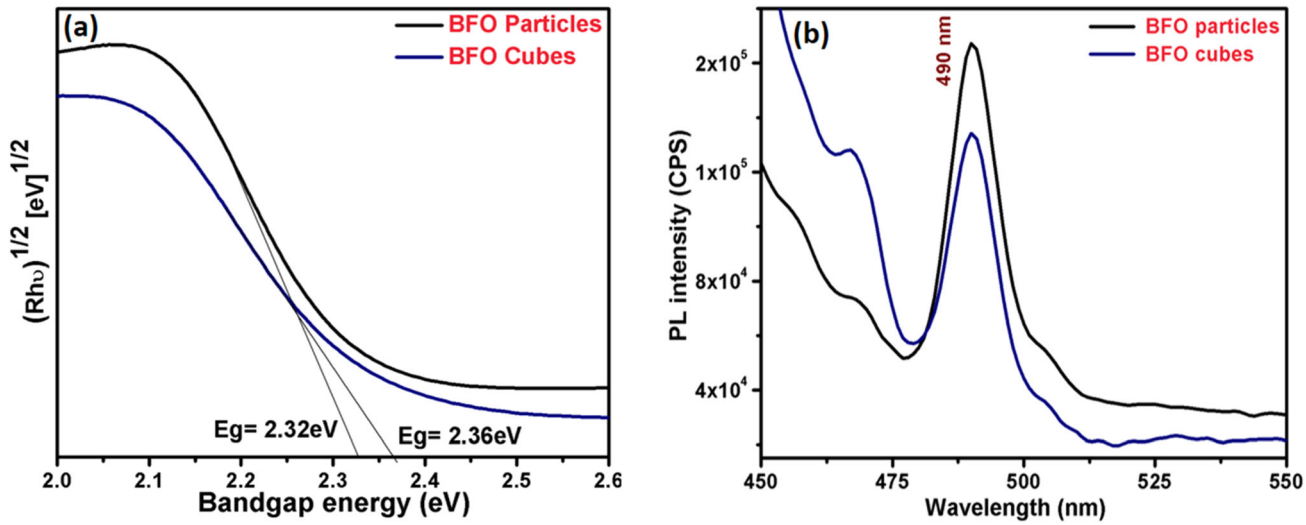

Fig. 4 **a** Estimation of bandgap energy using Kubelka–Munk plot and **b** PL spectrum of BFO particles and cubes

an increased bandgap energy in the system [41, 42]. It should be noted that the band structure engineering in photocatalytic material is essential in order to enhance the degradation efficiency via reducing or delaying the recombination rate of the excited charge carriers and it can be effectively done through discrete energy levels rather than the materials with defective or mid-valence band structures in the system.

The photoluminescence spectroscopy (PL) is employed as a tool to investigate the photophysical property of the systems as the PL intensity directly associates with charge carrier recombination process. The PL spectrum of BFO particles and cubes as shown in Fig. 4b is obtained at an excitation wavelength of 440 nm at RT (room temperature). The PL peak at 490 nm can be assigned to the emission via radiative process during the charge recombination in BFO [43]. From the results, it can be noted that there is reduction in the intensity of PL peak for BFO cubes as compared to particles. This reduced PL intensity can be assigned to the delayed charge recombination in the system, which can be owing to the enhanced electron delocalization in conduction band (CB) of BFO cubes as compared to particles. The reduction in recombination process can be directly assigned to its enhanced photocatalytic properties as discussed in the following section.

3.5 Photocatalytic properties

Photocatalytic performance of the prepared BFO particles and cubes is analyzed toward their ability of degrading the methylene blue (MB) dye under the sunlight irradiation. The obtained degradation spectra, C/C_0 plot, rate kinetics, and photocatalytic recyclability results are displayed in Fig. 5a–d, respectively. It can be seen in the C/C_0 plot that the BFO particles and cubes degraded around 73.2 and 99.6% of MB dye, respectively, at the end of 3 h of sunlight illumination. However, in total of the observed degradation percentage, around 8 and 21%, respectively, can be accounted for the dye removal via adsorption process as it can be seen some reduction in C/C_0 ratio under dark condition. The enhanced photocatalytic property of BFO cubes could be attributed to their cubic morphology-mediated photocatalytic efficiency in the system. Morphology of a photocatalyst could be one of the factors governing toward improving the photocatalytic property as it associates with other intrinsic properties such defects-free nature, existence of abundant reactive sites, improved charge separation, and higher recombination resistance [44]. Accordingly, it can be corroborated from XRD and XPS results that the BFO cubes are relatively defects-free in nature and possess more reactive sites due to their uniform shape and sharp edges along with higher surface energy as compared to particles. Furthermore, the observed reduced PL intensity indicated that the charge separation and recombination resistance could be high in

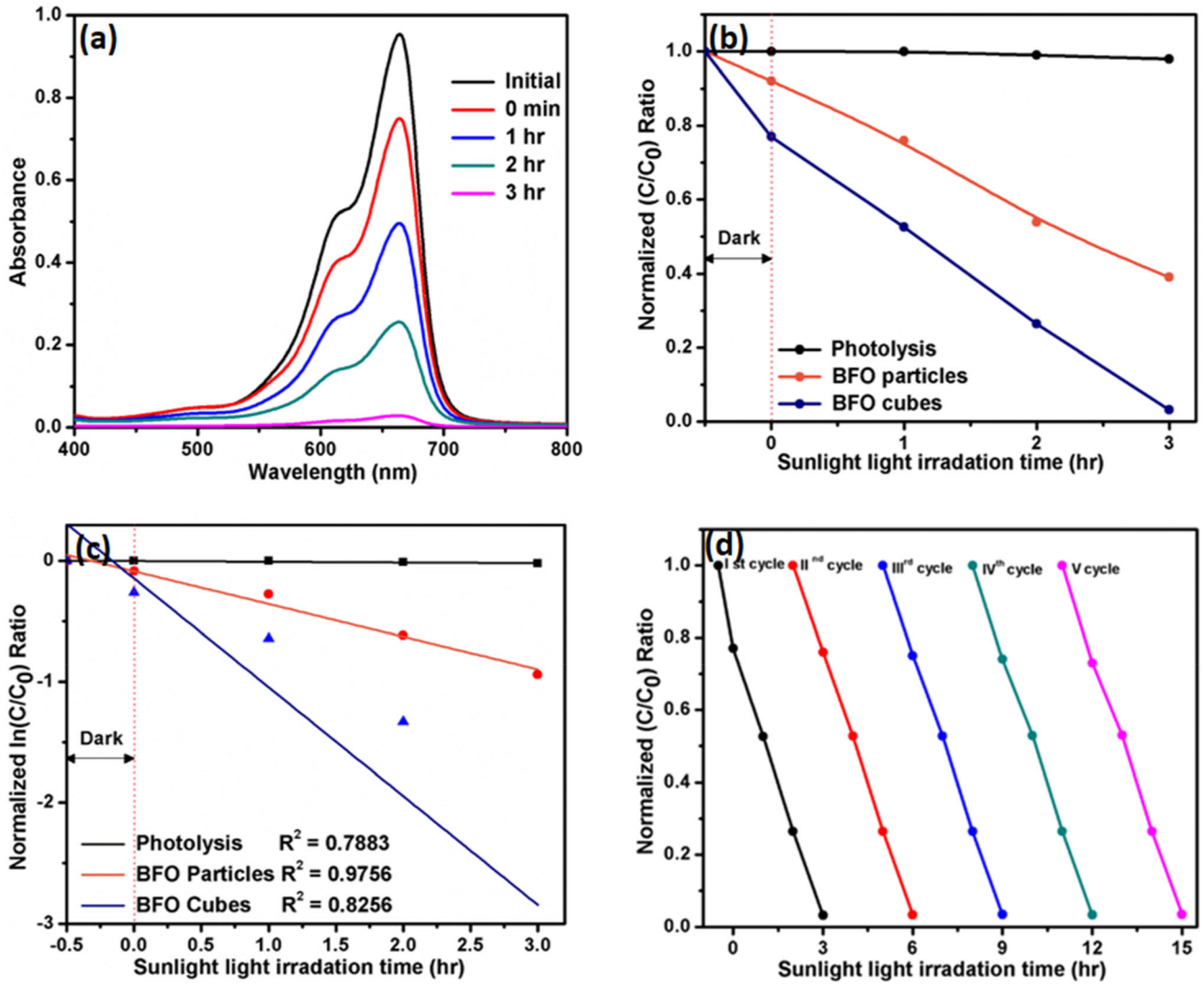

Fig. 5 **a** Photocatalytic degradation of MB dye, **b** C/C0 plot, **c** degradation rate kinetics, and **d** photocatalytic recyclability of BFO cubes

BFO cubes as compared to BFO particles. Therefore, the observed improved degradation ability of BFO cubes could be attributed to their morphology-driven enhanced properties facilitated by the egg white synthesis process.

Further, in order to investigate the degradation mechanism, the radicals which are responsible for degradation of MB is identified via radical scavenging analysis. In this analysis, the scavengers such as iso-propanol (IPA), ethylenediamine tetra acetic acid (EDTA), and p-benzoquinone (BQ) were taken to scavenge hydroxyl radicals ($^{\cdot}OH$), holes (h^{+}), and superoxide ($O_2^{\cdot -}$) anions, respectively, which evolve during the photocatalytic reactions. The obtained results are displayed in Fig. 6a and it showed that the degraded percentage of MB in the presence of these scavengers is in the order of BQ > EDTA > IPA. These observations indicate that the photocatalytic degradation of MB dye is largely driven by hydroxyl radicals as the degradation is largely decreased in the presence of IPA. This implies that the produced hydroxyl radicals are captured by IPA rather than involving in the degradation of the MB dye molecules. Therefore, the radical responsible for the degradation could be hydroxyl radicals over the other reactive species such as holes and superoxide anions. However, it should be noted that followed by IPA, the degradation percentage was decreased in the presence of EDTA as well. This can be attributed that the holes can also be the effective species involving the direct oxidation of MB dye during the photocatalytic degradation process.

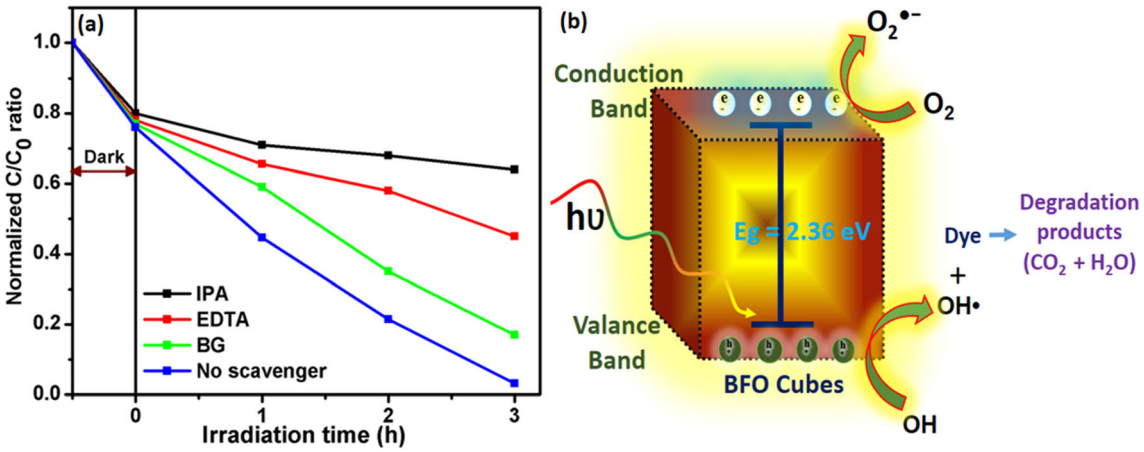

Fig. 6 **a** Scavenger test and **b** photocatalytic mechanism of BFO cubes

Based on these observations, a plausible photocatalytic mechanism can be proposed as follows. Upon the solar irradiation, the electrons in the valence band (VB) are excited to the conduction band (CB) creating holes (h^+) in the VB. These separated carriers further involve in the reactions as shown in Eq, (1)-(4), where the produced holes (h^+) oxidize the water molecules to produce hydroxyl radicals ($^{\cdot}OH$) and they also directly oxidize the MB molecules and lead to their degradation under solar irradiation [45, 46].

$$BiFeO_3 + hv \rightarrow e_{cb}^- + h_{vb}^+ \quad (2)$$

$$h_{vb}^+ + OH^- \rightarrow {}^{\cdot}OH \quad (3)$$

$$e_{cb}^- + O_2 \rightarrow O_2^{\cdot -} \quad (4)$$

$$Dye + {}^{\cdot}OH \rightarrow Dye'^{\cdot} + CO_2 + H_2O \quad (5)$$

$$Dye + h_{vb}^+ \rightarrow Dye^{\cdot} \rightarrow \text{degradation products} \quad (6)$$

$$Dye + O_2^{\cdot -} \rightarrow Dye^{\cdot} \rightarrow \text{degradation products} \quad (7)$$

The proposed photocatalytic mechanism is schematically represented in Fig. 6b, where the observed degradation efficiency is mediated via the collective oxidation by $^{\cdot}OH$ radicals and holes, which are abundantly produced in BFO cubes due to their improved charge separation, recombination resistance, rich surface-reactive sites, and defect-free nature attributed to their cubic morphology-induced discrete band energy structures in the BFO system, derived by the egg white-mediated synthesis process. Further, the performed photocatalytic recyclability test showed a consistent degradation of MB dye up to 5 cycles with negligible decrement in the degradation percentage. This indicates that the BFO cubes are photochemically stable and can be effectively employed for durable photocatalytic degradation applications under solar irradiation.

4 Conclusion

Bismuth ferrite particles with irregular and cubic morphology were synthesized by conventional and egg white-mediated sol–gel process, respectively. The $BiFeO_3$ (BFO) phase of both samples was confirmed via XRD technique and the irregular and cube-like morphology of the obtained material was confirmed using FESEM images with particle size in the range of 250–500 (for particles) and 80–200 nm (for cubes). The estimated bandgap energy of BFO particles and cubes was found to be around 2.32 and 2.36 eV, respectively, where the increased bandgap energy for BFO cubes was attributed to their discrete energy levels due to their cubic morphology with relatively uniform in shape. XPS studies revealed that the chemical oxidation state of Bi/Fe and O in the $BiFeO_3$ is + 3 and -2, respectively, which indicated their stoichiometric formation of the $BiFeO_3$ phase. However, the core-level spectra of Fe and O indicated that there could be oxygen vacancies in BFO particles, while the cubes were free from such defects. The PL results indicated that there could be relatively slower recombination process taking place in BFO cubes as compared to particles. The photocatalytic efficiency of BFO cubes (99.6%) was found to be greater than the particles (73.2%) at the end of 3 h, which attributed to their cubic morphology-induced enhanced charge separation, recombination resistance, surface-active sties, and discrete band energy structure in

BFO system. The observed recyclability of BFO cubes indicated that they can be potentially employed for a durable photocatalytic process toward degradation of dyes under solar irradiation.

Acknowledgements

The authors appreciatively acknowledge the CSIR (Council of Scientific & Industrial Research) for funding (09/115/(0783)/2018-EMR-I dt.13-04-2018) and thankfully acknowledge the MHRD-NCNSNT for Instrument facility to perform the part of research work.

Author contributions

SB and SB contributed to conceptualization; SB and MS contributed to data curation, formal analysis, and investigation : SB contributed to funding acquisition, supervision, and writing-original draft ; SB, MS, and SB contributed to writing-review and editing .

Funding

Funding was provided by Council of Scientific and Industrial Research, India (09/115/(0783)/2018-EMR-I).

Data availability

The datasets generated during and/or analyzed during the current study are available from the corresponding author on reasonable request.

Declarations

Conflict of interest Authors do not have any potential conflicts of interest to declare (both financial and non- financial).

Research involving human and animal participants This research does not include any Human participants and/or Animals.

References

1. W. Jiagang, F. Zhen, X. Dingquan, Z. Jianguo, W. John, Thin films and nanostructures. Progr. Mater. Sci. (2016). https://doi.org/10.1016/j.pmatsci.2016.09.001
2. W. Nan, L. Xudong, H. Lu, Z. Zhiqiang, Z. Renyun, O. HÃ¥kan, Y. Ya, Nanomicro Lett. **12**, 81 (2020). https://doi.org/10.1007/s40820-020-00420-6.
3. L. Shiva, S. Savita, T. Monika, G. Vinay, J. Phys. Chem. Solids (2020). https://doi.org/10.1016/j.jpcs.2020.109602
4. M. Nadeem, W. Khan, S. Khan, J. Mater. Sci. **31**, 11177–11194 (2020). https://doi.org/10.1007/s10854-020-03666-3
5. M. Sakar, S. Balakumar, P. Saravanan, S.N. Jaisankar, Mater. Res. Bull. **48**, 2878–2885 (2013). https://doi.org/10.1016/j.materresbull.2013.04.008
6. R. Zahra, K. Javad, M. Mohsen, H. Alireza, D. Abolfazl, Environ. Nanotechnol. Monit. Manag **11**, 100198 (2019). https://doi.org/10.1016/j.enmm.2018.100198
7. S. Bharathkumar, M. Sakar, N. Ponpandian, S. Balakumar, Mater. Res. Bull. **101**, 107–115 (2018). https://doi.org/10.1016/j.materresbull.2017.12.029
8. M. Sakar, S. Balakumar, P. Saravanan, S. Bharathkumar, Nanoscale **7**, 10667–10679 (2015). https://doi.org/10.1039/c5nr01079a
9. T. Rasheed, M. Bilal, F. Nabeel, M. Adeel, H.M. Iqbal, Environ. Int. **122**, 52–66 (2019). https://doi.org/10.1016/j.envint.2018.11.038
10. M. Patel, R. Kumar, K. Kishor, T. Mlsna, C.U. Pittman Jr., D. Mohan, Chem. Rev. **119**(6), 3510–3673 (2019). https://doi.org/10.1021/acs.chemrev.8b00299
11. I.O. Tijani, O.O. Fatoba, G. Madzivire, Water Air Soil Pollut. (2014). https://doi.org/10.1007/s11270-014-2102-y
12. A.D. Bokare, W. Choi, J. Hazard. Mater **275**, 121–135 (2014). https://doi.org/10.1016/j.jhazmat.2014.04.054
13. N.R. Reddy, U. Bhargav, M.M. Kumari, K.K. Cheralathan, M. Sakar, Int. J. Hydrog. Energy **45**, 7584–7615 (2020). https://doi.org/10.1016/j.ijhydene.2019.09.041
14. C.-C. Nguyen, M. Sakar, M.-H. Vu, T.-O. Do. Ind. Eng. Chem. Res **58**, 3698–3737 (2019). https://doi.org/10.1021/acs.iecr.8b05792
15. S. Bharathkumar, M. Sakar, K.R. Vinod, S. Balakumar, Phys. Chem. Chem. Phys. **17**, 17745–17754 (2015). https://doi.org/10.1039/c5cp01640a
16. A. Haruna, I. Abdulkadir, S.O. Idris, Heliyon (2020). https://doi.org/10.1016/j.heliyon.2020.e03237
17. S. Bharathkumar, M. Sakar, M. Navaneethan, J. Archana, Mater. Lett. **304**, 130475 (2021). https://doi.org/10.1016/j.matlet.2021.13047

18. S. Bharathkumar, M. Sakar, S. Balakumar, J. Phys. Chem. C **120**(33), 18811–18821 (2016). https://doi.org/10.1021/acs.jpcc.6b04344
19. K. Chybczyńska, P. Lawniczak, B. Hilczer, B. Leska, R. Pankiewicz, A. Pietraszko, L. Kępiński, T. Kałuski, P. Cieluch, F. Matelski, B. Andrzejewski, J. Mater. Sci. **49**, 2596–2604 (2014). https://doi.org/10.1007/s10853-013-7957-6
20. B. Kharisov, Recent Pat. Nanotechnol. **2**, 190–200 (2008). https://doi.org/10.2174/187221008786369651
21. C. Nandhini, S. Balakumar, AIP Conf. Proc. **2265**, 030636 (2020). https://doi.org/10.1063/5.0016805
22. F.C. Lü, K. Yin, K.X. Fu, Y.N. Wang, J. Ren, Q. Xie, Ceram. Int. **43**(18), 16101–16106 (2017). https://doi.org/10.1016/j.ceramint.2017.08.171
23. R. Syed, U. Muhammad, B.Z.U. Din, A.S. Ullah, M.A. Rehman, AIP Adv. **9**, 055025 (2019). https://doi.org/10.1063/1.5095468
24. N.B. Delfard, H. Maleki, A.M. Badizi, M. Taraz, J. Super Cond. Nov. Magn **33**(4), 1207–1214 (2020). https://doi.org/10.1007/s10948-019-05294-3
25. R. Radha, Y.R. Kumar, M. Sakar, K.R. Vinod, S. Balakumar, Appl. Catal. B **225**, 386–396 (2018). https://doi.org/10.1016/j.apcatb.2017.12.004
26. X. Liu, K. Li, C. Wu, Y. Zhou, C. Pei, Ceram. Int. **45**(18), 23869–23889 (2019)
27. Z. Sabouri, A. Akbari, H.A. Hosseini, M. Khatami, M. Darroudi, Polyhedron **178**, 114351 (2020). https://doi.org/10.1016/j.poly.2020.114351
28. S. Ahmed, Annu, S. Ikram, S. Y. Salprima, J. Photochem. Photobiol. B. S1011–1344(16) 30132–4 (2016). https://doi.org/10.1016/j.jphotobiol.2016.04.034
29. N.V. Kalpana, V.D. Rajeswari, Bioinorg. Chem. Appl. (2018). https://doi.org/10.1155/2018/3569758
30. M. He, P. Luo, J. Hong, X. Wang, H. Wu, R. Zhang, F. Qu, Y. Xiang, W. Xu, ACS Omega **4**(1), 2377–2386 (2019). https://doi.org/10.1021/acsomega.8b03224
31. A. Albanese, S.P. Tang, C.W.W. Chan, Annu. Rev. Biomed. Eng. **14**(1), 1–16 (2012). https://doi.org/10.1146/annurev-bioeng-071811-150124
32. Q.J. Ángel, K.V. Vignaswaran, D. Marco, A. Miguel, C. Alicia, Materials **12**, 1515 (2019). https://doi.org/10.3390/ma12091515
33. S.N. Tripathy, K.K. Mishra, S. Sen, B.G. Mishra, D.K. Pradhan, R. Palai, J. Appl. Phys. **114**, 144104 (2013). https://doi.org/10.1063/1.4824061
34. A.A.C. Carraro, Sci. Agric. **63**, 291–298 (2006). https://doi.org/10.1590/S0103-90162006000300013
35. A.C.C. Alleoni, A.J. Antunes, Rev. Bras. Cienc. Avic **6**, 77–82 (2004)
36. H. Yongming, F. Linfeng, Z. Yiling, Y. Jikang, W. Yu, G. Haoshuang, J. Nanomater. **2011**, 1–6 (2011). https://doi.org/10.1155/2011/797639
37. S. Bharathkumar, M. Sakar, J. Archana, M. Navaneethan, S. Balakumar, Chemosphere **284**, 131280 (2021). https://doi.org/10.1016/j.chemosphere.2021.131280
38. K.R. Vinod, P. Saravanan, M. Sakar, S. Balakumar, RSC Adv. **6**, 45850–45857 (2016). https://doi.org/10.1039/c6ra04935d
39. S. Pillai, D. Bhuwal, T. Shripathi, J. Mater. Sci. **24**, 2950–2955 (2013). https://doi.org/10.1007/s10854-013-1196-0
40. Y.L. Han, W.F. Liu, P. Wu, X.L. Xu, M.C. Guo, G.H. Rao, S.Y. Wang, J. Alloys Compd. **661**, 115–121 (2016). https://doi.org/10.1016/j.jallcom.2015.11.157
41. D.T. Kumar, S. Sweta, A.S.K. Sinha, Inorg. Chem. Commun. **117**, 107945 (2020). https://doi.org/10.1016/j.inoche.2020.107945
42. S. Jayababu, M. Inbasekaran, N. Sobana, Inorg. Chem. Commun. (2020). https://doi.org/10.1016/j.inoche.2020.108306
43. M.S. Akter, W. Zhiliang, L. Tongen, C. Peng, L. Bin, W. Lianzhou, Chem. Commun. (2020). https://doi.org/10.1039/d0cc04455e
44. B. Wang, J. Liu, S. Yao, F. Liu, Y. Li, J. He, M. Wang, J. Mater. Chem. **9**, 17143–17172 (2021). https://doi.org/10.1039/d1ta03895h
45. H.R. Chandan, M. Sakar, M. Ashesh, T.M. Ravishankar, T. Ramakrishnappa, R.T. Sergio, R.G. Balakrishna, Mater. Res. Bull. **104**, 212–219 (2018). https://doi.org/10.1016/j.materresbull.2018.04.014
46. V.R. Preethi, S. John, G. Bhalerao, B. Gupta, J. Singh, S. Singh, Solid State Sci. **109**, 106450 (2020). https://doi.org/10.1016/j.solidstatesciences.2020.106450